Multi-scale mechanical and morphological characterisation of sintered porous magnesium-based scaffolds for bone regeneration in critical-sized defects

Roxane Bonithon [a], Alexander Peter Kao [a], Marta Peña Fernández [a], Joseph Nicholas Dunlop [b], Gordon William Blunn [c], Frank Witte [d,e], Gianluca Tozzi [a*]

[a] Zeiss Global Centre, School of Mechanical and Design Engineering, University of Portsmouth, Anglesea Road, PO1 3DJ Portsmouth, United Kingdom
[b] School of the Environment, Geography & Geosciences, University of Portsmouth, Burnaby Road, PO1 3QL, Portsmouth, United Kingdom
[c] School of Pharmacy and Biomedical Sciences, University of Portsmouth, White Swan Road, PO1 2DT, Portsmouth, United Kingdom
[d] Department of Prosthodontics, Geriatric Dentistry and Craniomandibular Disorders, Charité - Universitätsmedizin Berlin, Aßmannshauser Straße 4-6, 14197 Berlin, Germany
[e] Biotrics bioimplants AG, Ullsteinstr. 108, 12109 Berlin, Germany

[*] Corresponding author. Phone: +44 23 9284 2514. E-mail: gianluca.tozzi@port.ac.uk.

Keywords: Magnesium alloys, Bone regeneration, *in situ* mechanics, X-ray computed tomography (XCT), digital volume correlation (DVC), scanning electron microscopy (SEM), electron backscatter diffraction (EBSD), nanoindentation.

Abstract

Magnesium (Mg) and its alloys are very promising degradable, osteoconductive and osteopromotive materials to be used as regenerative treatment for critical-sized bone defects. Under load-bearing conditions, Mg alloys must display sufficient morphological and mechanical resemblance to the native bone they are meant to replace to provide adequate support and enable initial bone bridging. In this study, unique highly open-porous Mg-based scaffolds were mechanically and morphologically characterised at different scales. *In situ* X-ray computed tomography (XCT) mechanics, digital volume correlation (DVC), electron microscopy and nanoindentation were combined to assess the influence of material properties on the apparent (macro) mechanics of the scaffold. The results showed that Mg exhibited a higher connected structure ($38.4mm^{-3}$ and $6.2mm^{-3}$ for Mg and trabecular bone (Tb), respectively) and smaller spacing (245µm and 629µm for Mg and Tb, respectively) while keeping an overall appropriate porosity of 55% in the range of trabecular bone (30-80%). This fully connected and highly porous structure promoted lower local strain compared to the trabecular bone structure at material level (i.e. -22067 ± 8409με and -40120 ± 18364με at 6% compression for Mg and trabecular bone, respectively) and highly ductile mechanical behaviour at apparent level preventing premature scaffold failure. Furthermore, the Mg scaffolds exceeded the physiological strain of bone tissue generated in daily activities such as walking or running (500-2000με) by one order of magnitude. The yield stress was also found to be close to trabecular bone (2.06MPa and 6.67MPa for Mg and Tb, respectively). Based on this evidence, the study highlights the overall biomechanical suitability of an innovative Mg-based scaffold design to be used as a treatment for bone critical-sized defects.

1. Introduction

Bone has a very efficient healing process that usually leads to a complete repair without the need for external medical contribution [1]. However, high-energy trauma, disease, tumour resection or osteomyelitis represent extreme bone healing clinical conditions leading to critical-sized defects that can cause non-union [2]. To address this clinical issue, different bone repair methods have been developed where autologous bone grafts have been considered the gold-standard [3,4]. However, bone grafts bring their share of unwanted effects such as donor-site morbidity, disease transmission, immune-mediated rejection, high non-union rate and limited availability [2,5]. To meet the growing demand in non-union defect treatment, biodegradable materials have been developed, offering a temporary solution able to maintain the mechanical integrity of the injured site while new bone is forming [6]. Currently, bone substitute materials mainly include calcium-phosphate (CaP) [7], bioglass [8] and natural or synthetics polymers, also including hydrogels [9]. These materials have been extensively investigated for bone tissue engineering due to their high bioactivity [2]. Nevertheless, their relatively low strength and brittle behaviour leading to premature scaffold failure, their unsuitable degradation rate and the difficulty to customize their apparent (macro) structure to resemble trabecular bone represent major limitations to their use in critical-sized bone defects [10].

Mg-based alloys represent a promising compromise between biocompatibility, bone regeneration ability and appropriate mechanical properties [11,12]. Mg, being the fourth most abundant cation in the human body, is involved in many biological functions (e.g. ion transport, enzymatic reactions or cell proliferation) and its physiological concentration is accurately regulated [13,14]. Consequently, the common side-effects induced by metallic biomaterials such as cytotoxicity, inflammation, cardiac and nervous system damage or implant removal [15–17], have not been found following Mg-based materials implantation. The *in vivo* efficacy of Mg in promoting bone regeneration has been extensively documented [18–22] and after 12 weeks of implantation, newly formed bone tissue is generally observed, suggesting enhanced bone mineralization and remodelling. In addition to its bone regeneration ability, the density (1.74-2.0g.cm^{-3}) and Young's modulus (41-45GPa) of Mg [6] appear to be closer to those of bone (1.8-2.1g.cm^{-3} and 3-20GPa) than the majority of other biomaterials. This aspect is fundamental to promote a suitable mechanical support until the bone regains enough strength; thus, limiting premature failure [10] and ensuring improved load transfer while avoiding stress-shielding [23].

However, it has been reported that the Mg-based alloy composition can greatly influence their mechanical behaviour [24,25]. In particular, zinc (Zn), another abundant essential nutrient in the human body, possesses a strengthening effect, able to improve the yield strength of Mg-based scaffolds [24]. The addition of manganese (Mn) has also shown an additional improvement in strength, while favourably decreasing the corrosion rate. Finally, some rare earth elements have been widely used in the composition of biodegradable Mg, such as yttrium (Y), able to refine the microstructure and also contribute to the mechanical properties [25]. The most widely studied Mg-based alloys can be divided into two groups, the AZ (Mg-Al-Zn system) and WE alloys (Mg-RE-Zr system) [12]. AZ alloys, mainly AZ31 (Mg-3Al-1Zn) and AZ91 (Mg-9Al-1Zn), showed enhanced mechanical performances [26]; however, their degradation rate has been found to be very high and aluminium is also known to induce toxicity at high doses [24]. WE alloys, mainly WE43 (Mg-4Y-3RE), are capable of forming a rare-earth (RE) oxide layer, which can improve biocorrosion resistance and biocompatibility [19]. The WZM211 (Mg-2Y-Zn-Mn) alloy proposed in this study aims to combine the mechanical and biological capabilities of these two groups through the addition of Zn to improve the mechanical performance and Y reducing the corrosion rate.

Mg, like most biomaterials, can be used to produce fixation devices (screws, plates or nails) to stabilize and enhance complex fracture healing [16,27] or porous scaffolds to promote bone regeneration in non-union defects [21]. Usually, porous Mg-based scaffolds are mechanically evaluated by uniaxial compression or tension [18,28,29] and although the stress-strain readings allow to investigate their overall mechanical behaviour (e.g. Young's modulus, yield stress), the local distribution and magnitude of the deformation that can lead to premature failure remains unexplored. Favourable local mechanics is crucial to achieve efficient load transfer and optimal overall mechanical performance as local strain accumulation has been found to promote the formation of microdamage (e.g. microcracks) reducing local mechanical efficiency and, consequently, overall mechanical properties [30]. *In situ* mechanics coupled with time-lapsed high-resolution X-ray computed tomography (XCT) and digital volume correlation (DVC) has emerged as a powerful and unique tool to quantify the three-dimensional (3D) full-field strain distribution in bones [31–34], cartilage-bone interface [35], biomaterials [36] and bone-biomaterial systems [30,37,38]. However, to the authors' knowledge, no studies have reported the local mechanical behaviour of open-porous Mg-based scaffolds using in situ XCT experiments and DVC.

The mechanical properties of scaffolds depend not only on their design and apparent structure, but also on the material properties. Nanoindentation is a robust testing methodology that has been widely used to measure local material properties of biomaterials [39] and bone tissue [40–42]. This technique has been already employed to characterise local mechanical variations related to the different components of Mg-based alloys [39], as well as to describe how *in vitro* corrosion reduces those mechanical properties [43–45]. Similarly, electron imaging techniques such as scanning electron microscopy (SEM) and electron backscatter diffraction (EBSD) have been proven highly beneficial in understanding the microstructural organisation and grain refinement of Mg-based materials following corrosion or manufacturing process [46,47]. However, a comprehensive multi-scale mechanical and structural evaluation of Mg-based materials, allowing to fully investigate their biomechanical performance as bone substitutes in critical-sized defects, is still missing as the majority of studies generally focused on a single level, either apparent [48,49] or micro [46].

Therefore, the aim of this study is to fully characterise the mechanical and morphological properties at different scales of a unique Mg-based scaffold composition to be used as a treatment for critical-sized bone defects. *In situ* XCT mechanics coupled with DVC was performed to assess the 3D full-field strain distribution and damage evolution in the Mg-based scaffolds as well as trabecular bone, which was used to provide a local mechanical comparison with the scaffold performance. This was coupled with electron microscopy-based imaging techniques (SEM/EDX/EBSD) and nanoindentation to further understand the influence of the Mg-based material properties on the apparent mechanical behaviour of the scaffold.

2. Methods

2.1. Sample preparation

The manufacturing process of porous Mg scaffolds has already been described elsewhere [18,50,51]. Briefly, the open-porous structures were manufactured from WZM211 Mg alloy (MgY2wt%Zn1wt%Mn1wt%) using single short fibres of approximately 4-8mm in length and 100-250µm in diameter. The fibres were fused by liquid phase sintering carried out at $10K.min^{-1}$ until 600°C, followed by further heating at $3K.min^{-1}$ until 628°C, held for 20 minutes. Cylindrical samples (55% porous) were then cut by CNC machines to obtain final dimensions of 8mm in diameter and 20mm in length.

Trabecular bone (Tb) samples were obtained from bovine proximal femurs. All surrounding soft tissues were removed and 20mm bone slices were cut perpendicularly to the physiological loading axis. Thereafter, 8mm diameter cylindrical cores (n=5) were extracted under copious water irrigation and then stored at -20°. In order to simulate the physiological conditions leading to scaffold implantation, bone specimens were cored near a bone defect (i.e. a cyst). Thus, two different bone structures were obtained, depending on their distance from the defect; away from the defect (~10-20mm), typical trabecular bone specimens were produced; closer to the defect (~1-5mm), the bone structure was more resembling a mix of trabecular and cortical bone, referred elsewhere as compact-coarse-trabecular bone (CCTb) [52]. Therefore, a direct comparison could be made between the porous Mg performance and that of trabecular or remodelled coarse-compact-trabecular bone, which represents the physiological response to specific mechanical demands generated by the presence of a bone defect.

2.2. *In situ mechanical testing and XCT imaging*

In order to minimize the influence of end-artifacts during mechanical testing [53], the two extremities of each Mg and bone specimens were embedded into endcaps (acetal for Mg and brass for bone) using a custom-made alignment system (Fig.1). The resulting specimens had a reduced-section gage length of approximately 15mm, close to a 2:1 ratio [30,37,54].
In situ uniaxial step-wise compression tests were conducted on n=5 Mg, n=3 trabecular bone (Tb) and n=2 compact-coarse-trabecular bone (CCTb) in a loading stage (CT5000 5kN, Deben Ltd, UK) fitted within the X-ray microscope chamber (Versa 510, Zeiss, US) with a speed rate of 0.1mm/min at room temperature (Fig.1). The bone specimens were kept hydrated in PBS solution throughout the duration of the test. A preload of 10N was first applied to ensure contact with the compression platens prior to testing; then, two repeated scans were acquired, without repositioning, for the estimation of the DVC strain uncertainty [55]. Mg specimens were tested at 1, 3, 6 and 10% apparent compression, whereas the bone cylinders were loaded up to 6% as a critical decrease of the strength (i.e. failure) was observed just after 3% compression.
Young's modulus was determined from the stress-strain curves by calculating the slope of the linear regression between σ_{30} or σ_{50}, for Mg and bone respectively, and σ_{80}, corresponding to 30, 50 and 80% of the ultimate stress. The correlation value (R^2) of the calculated slope was equal or superior to 98% in all cases [56]. The linear regression was then offset by 0.2% to calculate the yield stress. For each compression step high-resolution XCT was carried out at 60V and 4/5W or 80V and 7W for Mg and bone, respectively; 1601 projections were acquired over 360° with an exposure time of 5s or 3.5s (Mg and bone, respectively) per projection and the resulting tomograms had a voxel size of 20μm. All specimens were allowed to settle for 30 minutes prior to image acquisition to reduce imaging artifacts due to stress relaxation [32].
In order to better visualise the formation of microcracks, higher magnification scans were performed using a different loading stage (CT500 500N, Deben Ltd, UK), allowing higher XCT resolution on an additional Mg scaffold (n=1, 8mm diameter and 15mm length) and three additional Tb samples (4mm diameter and 10mm length). Images were acquired at 1, 3 and 6% compression for Tb and up to 10% for Mg targeting the centre of the structures and achieving a voxel size of 5μm for Mg and 3.5μm for the Tb with a 4s exposure time.

2.3. *Image post-processing*

The XCT datasets were rigidly registered using a correlative metric (Avizo 9.7, ThermoFisher Scientific, US) using the first preloaded image as a reference. Each image was cropped to include only the specimen's structures in the field of view (~8.4x8.4x10mm^3). On the resulting images, DVC was performed. Higher magnification images were subjected to extra filtering steps. Noise was first reduced by a non-local mean denoising filter [57]. Then, they were converted into binary images using Otsu's method [58] and isolated voxels were eliminated using an erosion module in Avizo followed by a dilatation operation. Finally, they were masked by multiplying the filtered image by the corresponding binary image. The resulting image contained the material (bone or Mg) surrounded by a "zero-value background" [59].

2.4. *Morphometry*

Morphometric parameters were computed in a smaller volume of interest (~6.6x6.6x10mm^3) of the preloaded 20μm voxel size tomograms, excluding the sample edges in order to further limit the side-artifacts occurring during sample manufacturing [60]. These cropped images were then converted to binary as described above.

Morphometric parameters, commonly computed to describe bone morphometry [61], were calculated for Mg, Tb and CCTb using the BoneJ plugin of Fiji software [62,63]; these are fibre/trabecular thickness (Th), fibre/trabecular spacing (Sp), solid volume fraction (SV/TV), solid surface density (SS/TV), solid specific surface (SS/SV), structure model index (SMI), degree of anisotropy (DA) and connectivity (Conn.D). The values are presented as mean ± standard deviation. Morphometric properties were also investigated using the pore network and volume fraction map modules of Avizo.

2.5. *Digital volume correlation (DVC)*

DVC (DaVis v10.0.5, LaVision Ltd, Germany) was performed between the first preloaded image and those at 1, 3, 6 and 10% compression to compute the 3D full-field third principal strain (ε_{p3}) of Mg, Tb and CCTb at different resolutions (20µm and 3.5-5µm voxel size) while being stepwise compressed *in situ* (Fig.1). DaVis software is based on a local approach of cross-correlation operating on the intensity values (grey-level) of the 3D images. Further details on the operating principles have already been reported elsewhere [31,59]. For both apparent and tissue levels, a multi-pass scheme with decreasing sub-volumes, from 128 to 48 voxels [64,65], and 0% overlap [55] were used, followed by a vector post-processing, where sub-volumes with a correlation coefficient below 0.6 were removed. Strain uncertainties were found to be below 300με in all cases for all specimens [55,59].

Based on the strain maps obtained by DVC, two volumes of interest (3mm^3) were extracted in both the highest (exceeding the absolute strain (ε_{p3}) of 40000με) and lowest (not exceeding the absolute strain (ε_{p3}) of 10000με) strain regions from each Mg sample (Fig.1). On every lowest and highest area, a local analysis was performed by computing the morphometric parameters with ImageJ as previously described in 2.4. This sub-level of investigation was carried out to detect local morphometric differences related to the strain variation for the Mg scaffolds.

2.6. *SEM, EDX and EBSD*

Microstructural studies were performed on the uncompressed (N=3) and compressed (N=3) Mg scaffolds to correlate the fibre microstructure to the mechanical behaviour at apparent level. The microstructure and composition were assessed by scanning electron microscopy (SEM - EVO MA10, Zeiss, US) coupled with energy-dispersive X-ray spectroscopy (EDX, X-Max 80, Oxford Instruments, UK). Then, electron backscatter diffraction (EBSD) was used to further understand grain texture and orientation (Nordlys Nano, Oxford Instruments, UK).

When preparing the samples for EBSD, a water-free procedure was employed [46]. The samples, either before or after compression, were first cut in two directions to expose the longitudinal or transverse sections of the fibres (Fig.1). They were then embedded into a low-viscosity resin (EpoThin 2, Buehler, USA) and polished with a polycrystalline diamond suspension (successively 6, 3 and 1µm) for approximately 5-8 minutes. Final polishing was executed using 0.05µm aluminium oxide powder for 20-30 minutes to achieve an optimal final polished surface for EBSD. A glycerol-based was employed as lubricant. Mg alloys possess a high affinity with oxygen [50], therefore to limit their oxidation in air they were kept in glycerol. Before imagining, glycerol was taken off with isopropanol and the microstructure was revealed by etching with a 1% nitric solution.

2.7. *Nanoindentation*

The embedded Mg samples, prepared for electron microscopy imaging, were used to further investigate the mechanical properties at the material level by nanoindentation. Nanoindentation tests were performed with a TI PREMIER indenter (Hysitron, Bruker Inc., US) equipped with a Berkovich tip. A matrix of 114 indents (square of 12x12) with a spacing of 6µm and 1000µN load control was applied on 6 fibres per specimen (uncompressed vs. compressed and longitudinal vs. transverse). The loading/unloading rate was set to 10mN/s with a holding time of 0.1s. The hardness (H) and the reduced elastic modulus (E_r) [66] were obtained with TriboScan software (TriboScan Professional, Hysitron, Bruker, US). The reduced modulus was finally converted to the indentation modulus (E_i) using equation (1):

$$E_i = \frac{1 - \nu^2}{\frac{1}{E_r} - \frac{1 - {\nu_t}^2}{E_t}}$$

where ν and ν_t refer to the Poisson's ratio of Mg and the Berkovich tip (0.261 and 0.07, respectively) and E_t to the Young's modulus of the Berkovich tip (1141GPa) [66,67]. The anisotropic ratio was also calculated for uncompressed and compressed conditions by dividing the indentation modulus and hardness of the transverse section by the longitudinal section (E_i/H).

2.8. Statistical analysis

Differences between the highest and lowest strain areas for the local morphometry and between the nanoindentation groups were tested using the Mann-Whitney U test. All statistics were performed using SPSS statistics (SPSS statistics 25, IBM, USA) and the significance level was α=0.05.

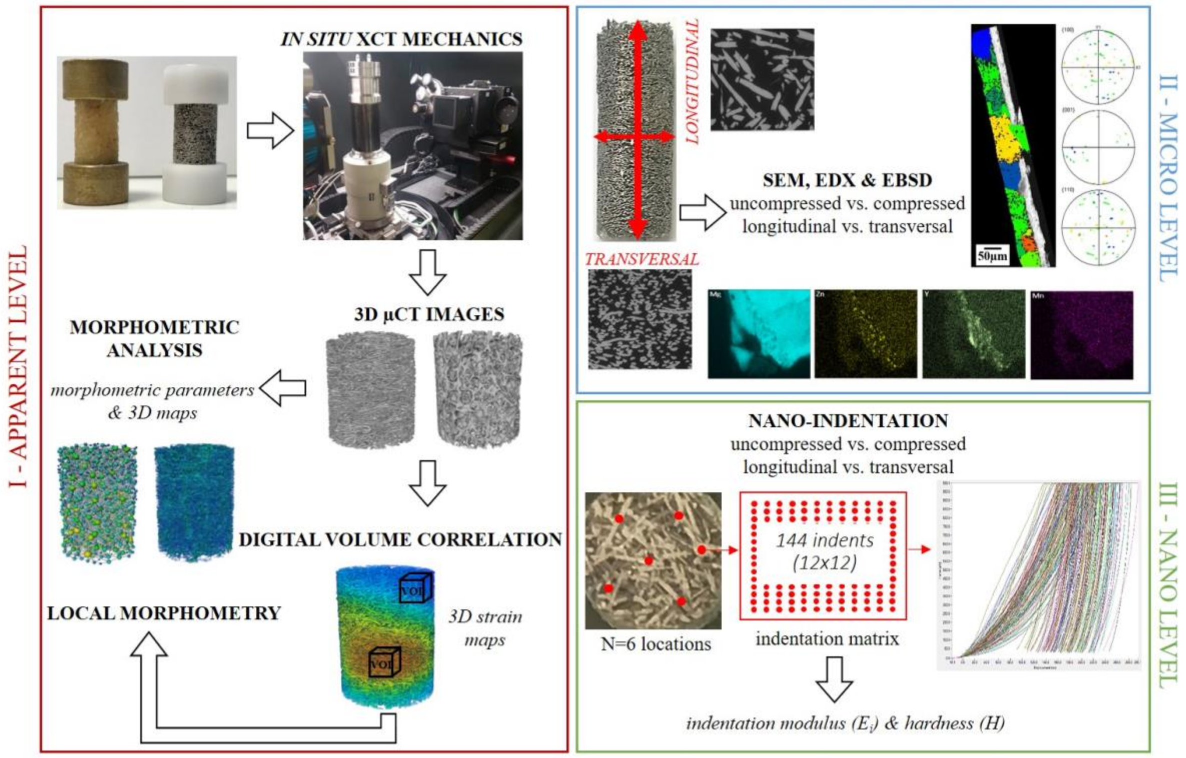

Fig.1. Schematic representation of the multi-scale analysis workflow at (I) apparent level including *in situ* XCT mechanics coupled with DVC and morphometric analysis of the overall structure (Mg and trabecular bone). (II) micro-level employing various electron-based imaging techniques (SEM, EDX and EBSD) to evaluate the incidence of the Mg fibre microstructure on the apparent behaviour and finally, (III) nano-level to understand the influence of Mg material properties, through nanoindentation, on the mechanical performance of the scaffold.

3. Results

3.1. Mechanical properties

The stress-strain curves of the Mg and bone specimens are shown in Fig.2. On the Mg curves, the linear elastic region could not be clearly identified. Then, around 4% compression it was rapidly followed by a long strain hardening where the stress still ramped up to 10% compression. Tb showed typical elastic-plastic behaviour, first a linear elastic region up to 3-4% compression, followed by a plateau and finally a prolonged softening with a reduction of the stress, corresponding to failure, up to 6% compression. Due to its more compact structure, CCTb did not display any stress reduction after yielding within the range of strain used, but rather a strain hardening region, as previously observed on the Mg curves.
Mg, Tb and CCTb yielded at the same compression stage (around 3-4%), whilst the stress reached by both Tb and CCTb was much higher than Mg (2.1 ± 0.9MPa, 6.7 ± 1.8MPa and 9.8 ± 1.0MPa for Mg, Tb and CCTb, respectively) (Table 1).

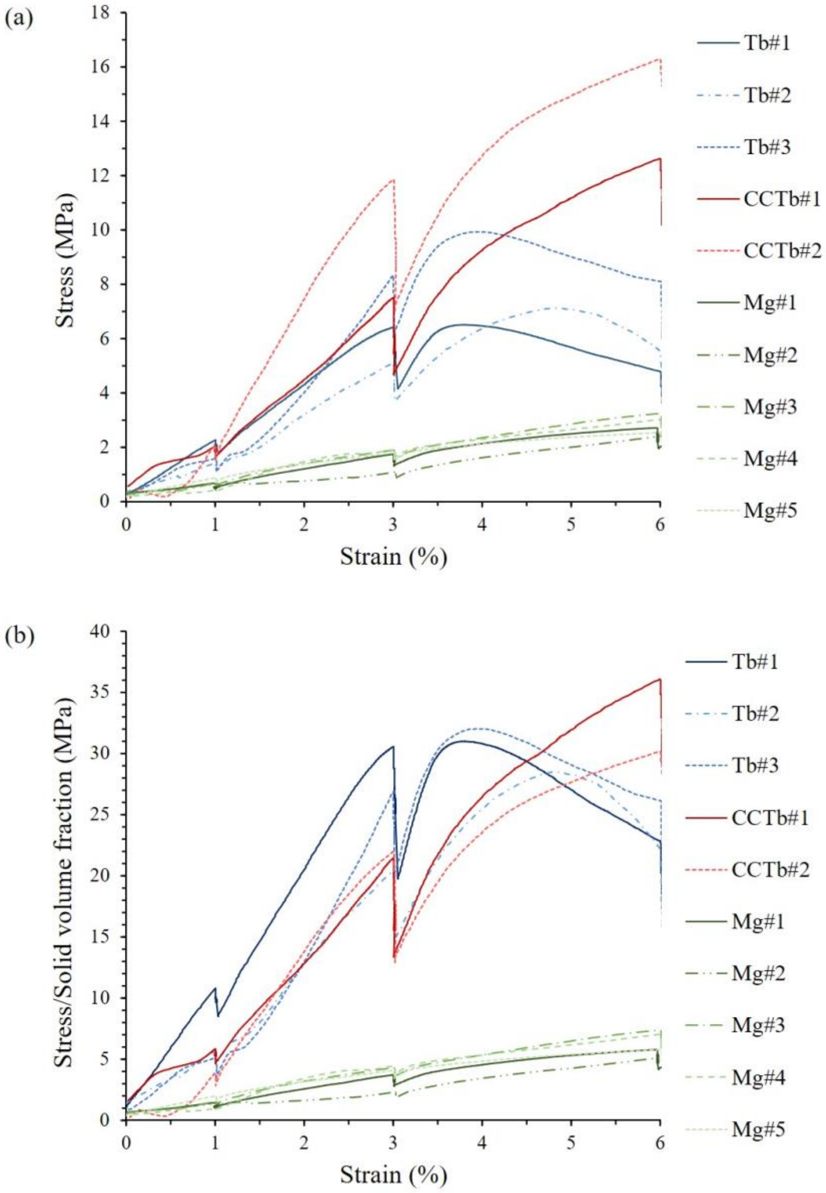

Fig.2. Compressive (a) stress-strain curves of magnesium (Mg), trabecular bone (Tb) and compact-coarse-trabecular bone (CCTb) and (b) normalized stress-strain curves where the stress is divided by the solid volume fraction.

Table 1. Mechanical properties of Mg, Tb and CCTb. Data are shown as mean ± SD.

	Mg	**Tb**	**CCTb**
Young's modulus E (GPa)	0.068 ± 0.028	0.293 ± 0.082	0.412 ± 0.148
Normalized Young's modulus (E/solid volume fraction)	0.153 ± 0.067	1.129 ± 0.180	0.895 ± 0.142
Yield stress σ (MPa)	2.06 ± 0.78	6.67 ± 1.75	9.77 ± 1.04
Normalized yield stress (σ/solid volume fraction)	4.37 ± 1.74	25.98 ± 5.01	22.48 ± 2.46

3.2. *Morphometry*

The morphometric parameters of Mg were comparable to those of Tb or CCTb, except for lower fibre/trabecular spacing and higher connectivity as reported in Table 2. In addition, fibre/trabecular spacing, solid volume fraction and solid surface density of Mg were closer to the CCTb values than those of Tb.

Table 2. 3D morphometric parameters of Mg, Tb and CCTb. Data are shown as mean ± SD.

	Mg	**Tb**	**CCTb**
Fibre/trabecular thickness (µm)	178 ± 2	195 ± 9	256 ± 76
Fibre/trabecular spacing (µm)	245 ± 11	629 ± 89	455 ± 36
Solid volume fraction	0.45 ± 0.02	0.26 ± 0.05	0.45 ± 0.13
Solid surface density (mm^{-1})	5.9 ± 0.2	3.8 ± 0.5	4.6 ± 0.2
Solid specific surface (mm^{-1})	13.1 ± 0.2	14.7 ± 1.1	10.9 ± 3.6
Structure model index	1.7 ± 0.4	2.2 ± 0.2	0.6 ± 1.2
Degree of anisotropy	2.2 ± 0.5	2.1 ± 1.0	3.1 ± 1.3
Connectivity (mm^{-3})	38.4 ± 2.4	6.2 ± 0.8	3.4 ± 0.9

This was also observed on the porous network (Fig.3II) where the pore distribution and diameter of Mg were more resembling CCTb. Mg and CCTb presented a majority of pores with a diameter ranging 500-600µm while the pores of Tb appeared larger, about 900-1000µm. In terms of local volume fraction (Fig.3III), all specimens exhibited a non-uniform distribution with areas of higher porosity (i.e. lower volume fraction). Comparing the pore network and volume fraction maps, it was found that these higher local porosities corresponded to a local accumulation of larger pores.

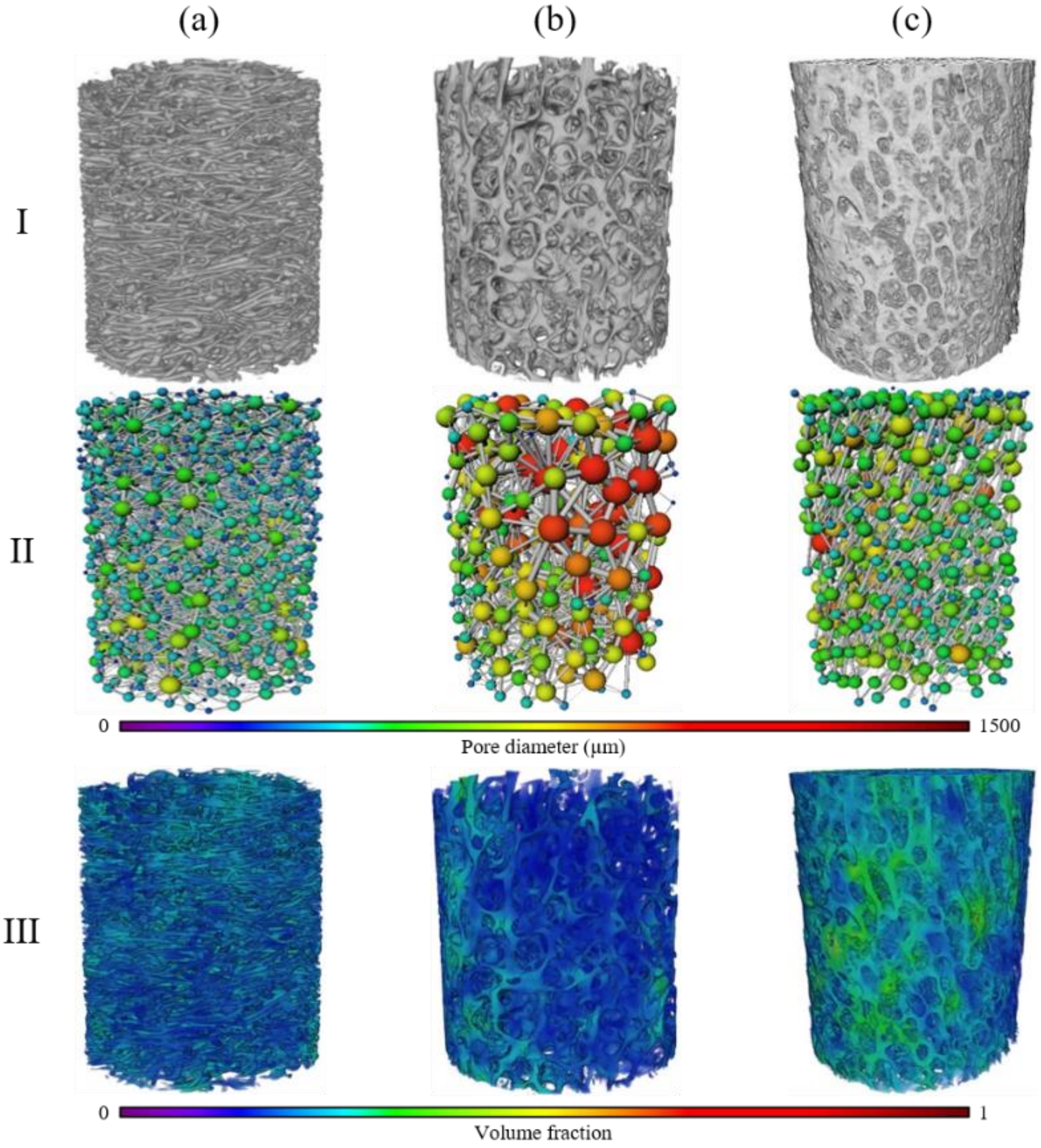

Fig.3. (I) XCT reconstruction, (II) 3D pore network and (III) volume fraction map for representative (a) Mg; (b) Tb and (c) CCTb specimens.

3.3. Digital volume correlation (DVC)

The full-field third principal strain (ε_{p3}) distribution at different compression stages is reported in Fig.4 and 5 for Mg, Tb and CCTb (20μm voxel size). Strain build-up was observed longitudinally in the centre of Mg and CCTb and transversally displaced to the periphery (Fig.4 and 5II). This strain distribution indicated that the structures were subjected to some buckling, which increased with further compression. It could be noticed how the strain distribution of Tb differed by being mainly localised in a central pack of trabeculae (Fig.5I) leading to a global failure (Fig.2). However, although the strain pattern of Mg was closer to CCTb, their magnitude varied widely. At 6%, Mg scaffolds locally reached -13658 ± 5485με, whilst CCTb reached -8564 ± 5801με and Tb -3005 ± 1308με.

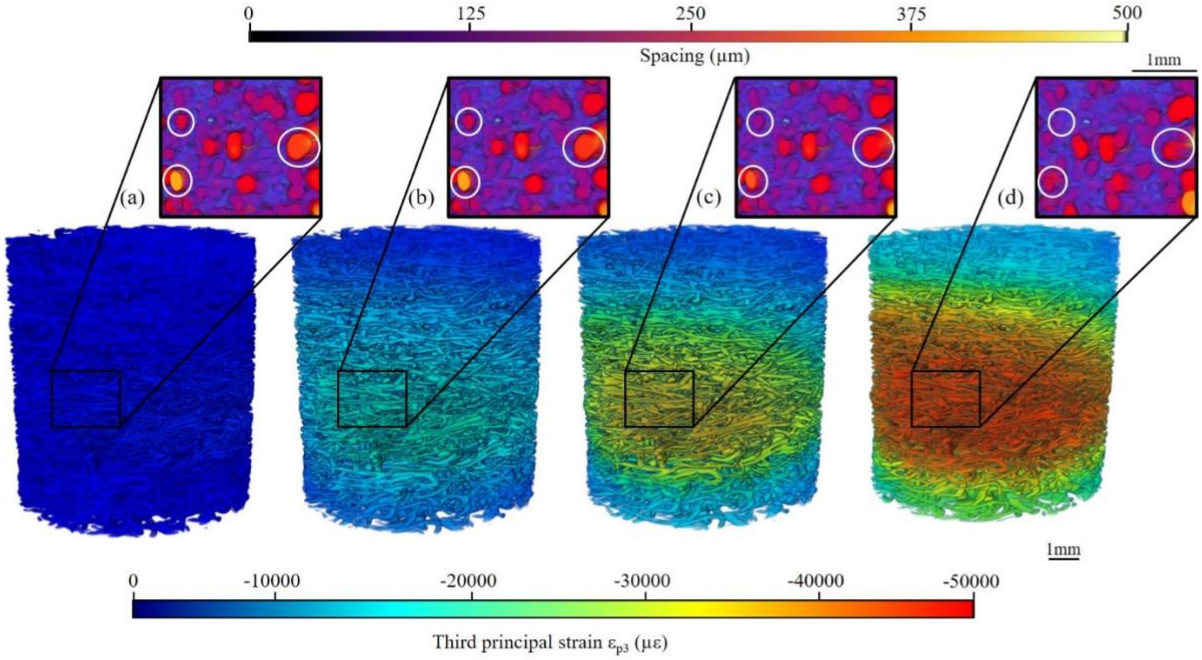

Fig.4. Full-field third principal strain (ε_{p3}) distribution and spacing maps where white ovals indicate partial pores closure (reduced local spacing) at (a) 1%, (b) 3%, (c) 6% and (d) 10% for a representative Mg scaffold (20μm voxel size).

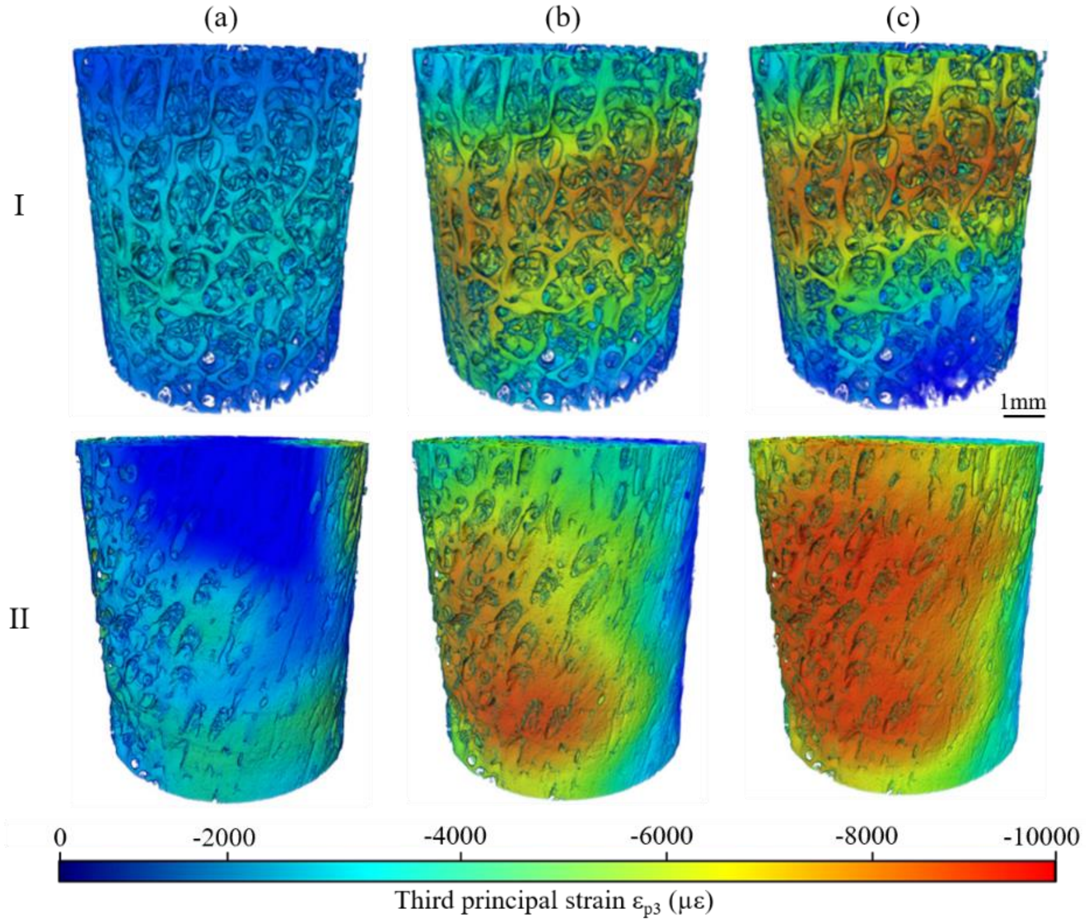

Fig.5. Full-field third principal strain (ε_{p3}) distribution at (a) 1%, (b) 3% and (c) 6% for a representative (I) Tb and (II) CCTb specimen (20μm voxel size).

Fig.6 shows the third principal strain (ε_{p3}) of Mg and Tb visualised at the fibre/tissue level (5 or 3.5µm voxel size). The strain pattern of Mg (-22067 ± 8409µε at 6% compression) appeared to be similar to that of the apparent level with one major deformation area gradually distributed throughout the whole structure, which increased with further compression. In contrast, the strain distribution of Tb (-40120 ± 18364µε at 6% compression) displayed multiple accumulation regions, where the presence of microcracks was observed at 6% compression corresponding to the apparent plastic region of the mechanical curves (Fig.2). Such microcracks were not visible on Mg.

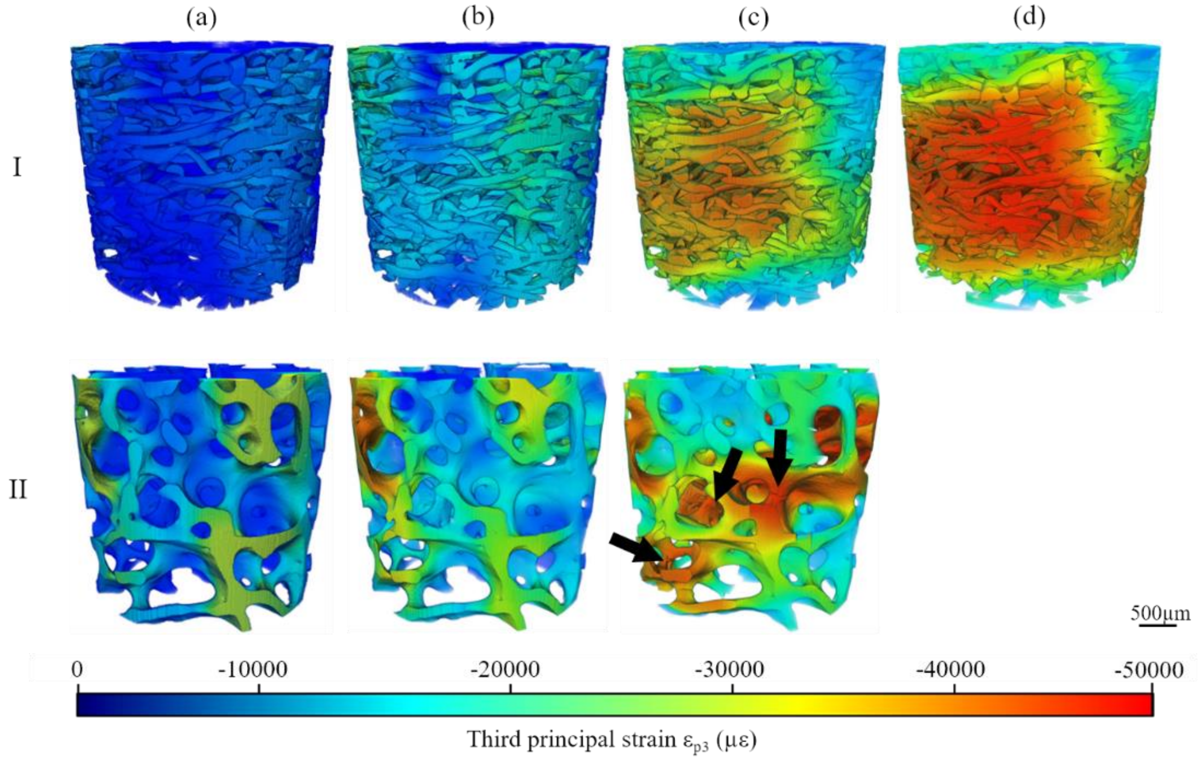

Fig.6. Full-field third principal strain (ε_{p3}) distribution at (a) 1%, (b) 3%, (c) 6% and (d) 10% for a representative (I) Mg (5µm voxel size) and (II) Tb (3.5µm voxel size) specimen. Microcracks in Tb at the final compression step (6%) are indicated by arrows.

As no microcracks were observed in the Mg scaffolds, a local morphometric analysis was carried out in order to explain its strain distribution. Based on the apparent full-field ε_{p3} maps (Fig.4), two regions called "high-strain" and "low-strain" were defined and their morphometric parameters were computed (Fig.1). The results are presented in Table 3. Although all morphometric parameters seemed to suggest a local increase in porosity in high-strain regions compared to low-strain ones (i.e. a decrease in solid volume fraction, 0.48 vs. 0.44, and connectivity, 45.1 mm^{-3} vs. 38.8mm^{-3} for low-strain compared to high-strain regions), only the fibre/trabecular spacing presented a significant difference with a reduction from 248µm in high-strain areas to 217µm in low-strain ones. Furthermore, in the high-strain regions, partial pore closure was observed (Fig.4) with an average reduction in spacing from 248 ± 11µm to 238 ± 7µm for preload and 10% compression, respectively.

Table 3. 3D morphometric parameters of high (exceeding the absolute strain of 40000$\mu\varepsilon$) vs. low (not exceeding the absolute strain of 10000$\mu\varepsilon$) strain areas of Mg, based on the DVC full-field ε_{p3} maps. Data are shown as mean ± SD. *$p<0.05$ when comparing low-strain to high-strain.

	High-strain	**Low-strain**
Fibre/trabecular thickness (µm)	174 ± 3	178 ± 39
Fibre/trabecular spacing (µm)	248 ± 22	217 ± 12*
Solid volume fraction	0.44 ± 0.03	0.48 ± 0.01
Solid surface density (mm^{-1})	6.0 ± 0.3	6.4 ± 0.2
Solid specific surface (mm^{-1})	13.7 ± 0.2	13.3 ± 0.6
Structure model index	1.9 ± 0.3	1.6 ± 0.1
Degree of anisotropy	2.8 ± 0.2	2.7 ± 0.3
Connectivity (mm^{-3})	38.8 ± 6.1	45.1 ± 7.0

3.4. SEM, EDX and EBSD

The SEM images before and after compression of the Mg scaffolds at different magnifications are reported in Fig.7. Fig.7a and b show how the fibres were randomly distributed to form a highly connected porous structure and no significant visual differences were observed before and after compression. At higher magnification, before compression, the surface of the fibres looked smooth and only a few large grains of about 50µm were detectable, as well as particle inclusions of about 2.3 ± 0.9µm. (Fig.7c). However, after compression, even though the grain sizes were similar, their boundaries were more visible. Two types of microdamage were identified at the fibre junction prior to compression (Fig.7e and g). The first type, containing a high concentration of particle inclusions, was oriented in a single direction parallel to the fibres, whereas the second type had multiple orientations. After mechanical testing, the grain boundaries were accentuated and developed typical ductile damage patterns. However, no additional microcracks were observed in the Mg scaffolds when compared to the undeformed stage.

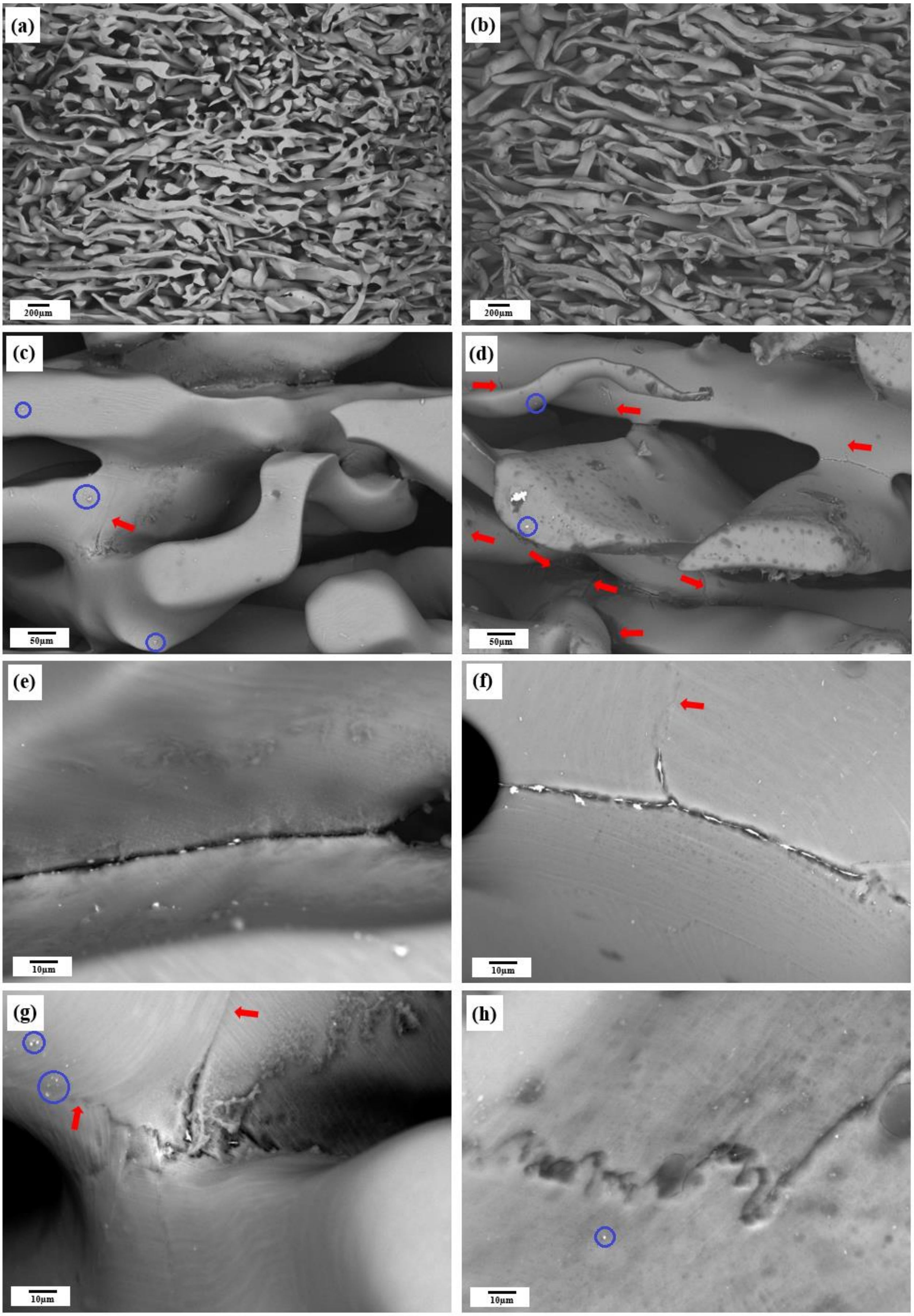

Fig.7. SEM images of Mg at different magnifications before (a,c,e,g) and after (b,d,f,h) mechanical testing. Grain boundaries are indicated by red arrows and particle inclusions by blue circles.

The EBSD results prior and post mechanical testing are detailed for the longitudinal (Fig.8) and transverse (Fig.9) sections of the Mg scaffolds. In the longitudinal section, both before and after compression, the fibres did not appear to be plastically strained. Moreover, no difference was observed in the distribution and magnitude of the degree of orientation of the grains after compression. However, in the transverse section, the grains were plastically deformed, even in the uncompressed condition. A slight increase in the degree of orientation of the grains was identified in the transverse section compared to the longitudinal one. On the maps (Fig.9g), it was also observed how the degree of orientation was higher at the fibre junctions after compression.

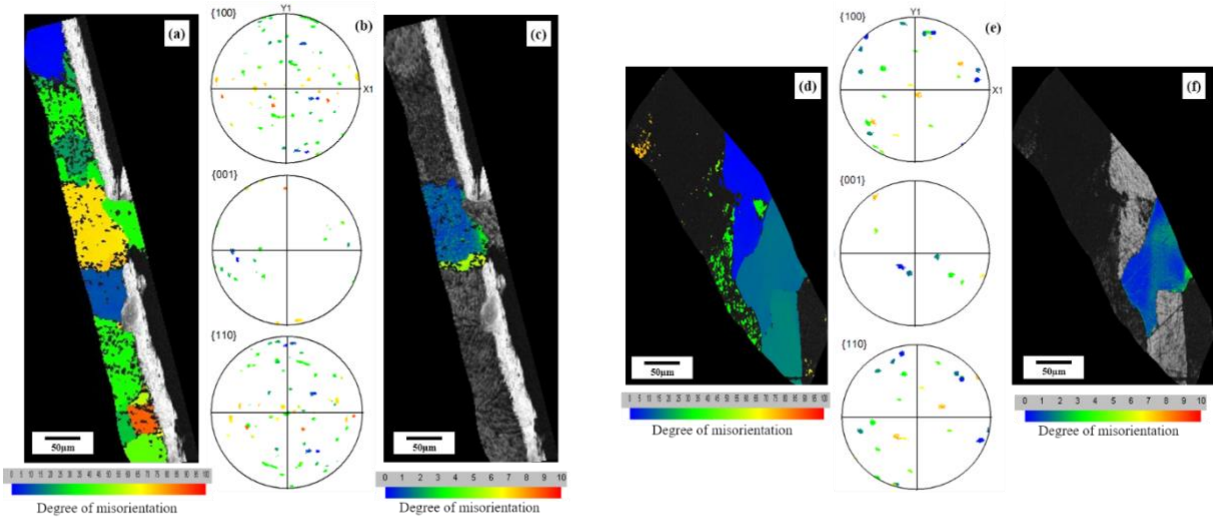

Fig.8. Microstructure and grain orientation of one fibre (a,d) with its corresponding pole figure (b,e) and orientation of one grain of the fibre (c,f), before (a,b,c) and after (d,e,f) mechanical testing in the longitudinal section.

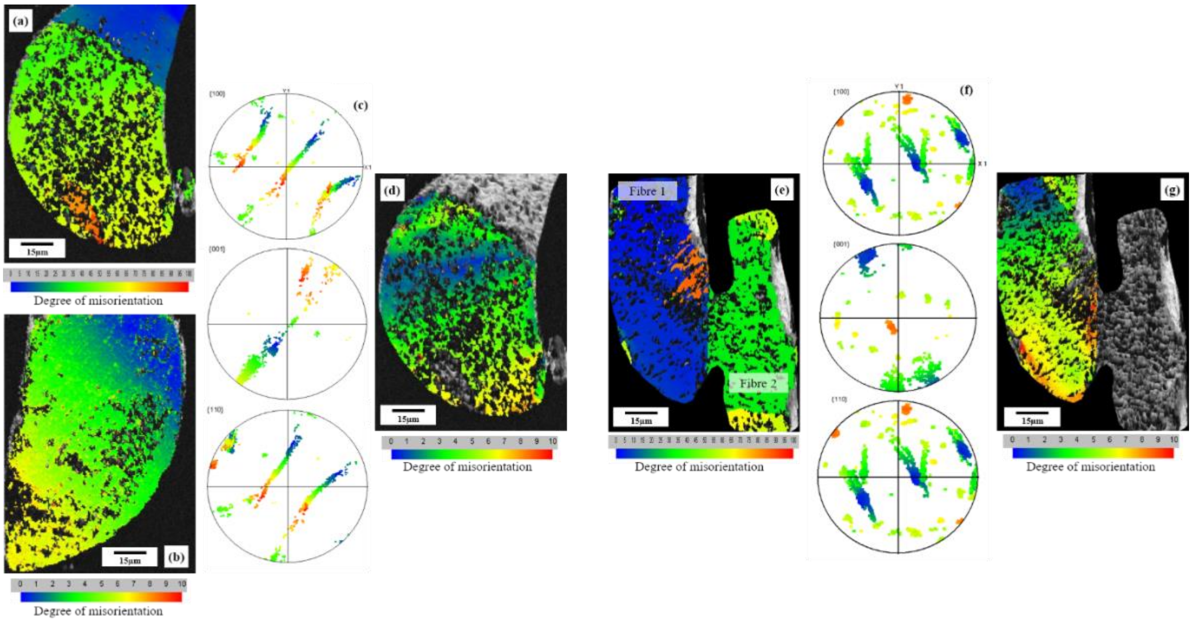

Fig.9. Microstructure and grain orientation of one (a and b) or two fibres (e) with its corresponding pole figure (c, f) and orientation of one grain of the fibre (d, g), before (a, b, c, d) and after (e, f, g) mechanical testing in the transverse section.

While the Mg content seemed to be uniformly distributed along the fibres, Zn, Y and Mn seemed to be more heterogeneous (Fig. 10). In specific areas, especially at the fibre junction and grain boundary, a higher concentration of Y and Zn was observed. Despite keeping the specimens in glycerol to avoid direct contact between Mg and air, oxygen was observed (10-15%) on the fibres, especially at the fibre/resin interface.

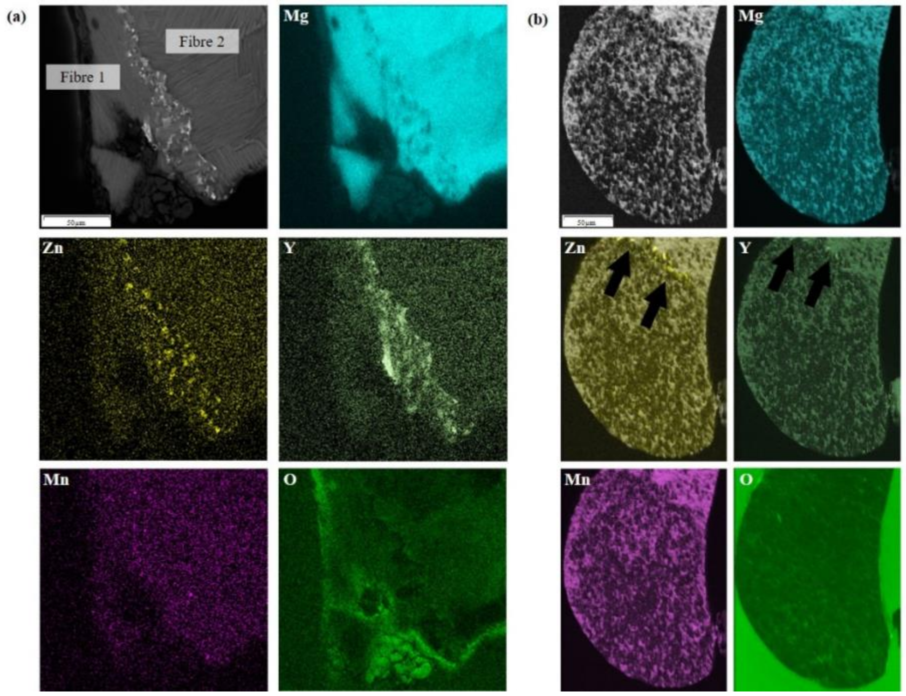

(c)

Element	At. %
Mg	**95.5**
Zn	**1.5**
Y	**2.3**
Mn	**0.7**

Fig. 10. EDX mapping of (a) the fibre junction where fibre 1 and fibre 2 are indicated, (b) the grain boundaries and (c) the percentages of alloying elements. Black arrows indicate the Zn-Y rich particles at the grain boundaries.

3.5. Nanoindentation

The indentation modulus (E_i) and hardness (H) in uncompressed and compressed Mg, for the longitudinal and transverse sections, are presented in Fig.11. Before compression, the transverse section exhibited a higher indentation modulus (37.29 ± 1.59GPa) and hardness (1.26 ± 0.10GPa) compared to the longitudinal (32.26 ± 3.38GPa and 1.06 ± 0.18GPa, for indentation modulus and hardness, respectively). This difference highlighted an anisotropic mechanical behaviour with an anisotropic ratio of 1.2.

A reduction in hardness and indentation modulus was noticed after compression in both sections (1.01 ± 0.21GPa and 31.05 ± 3.58GPa, 0.95 ± 0.01GPa and 30.09 ± 1.35GPa for the transverse and longitudinal sections, respectively). However, it seemed that this decrease affected the transverse section (reduction of 20%) more than the longitudinal (11%).

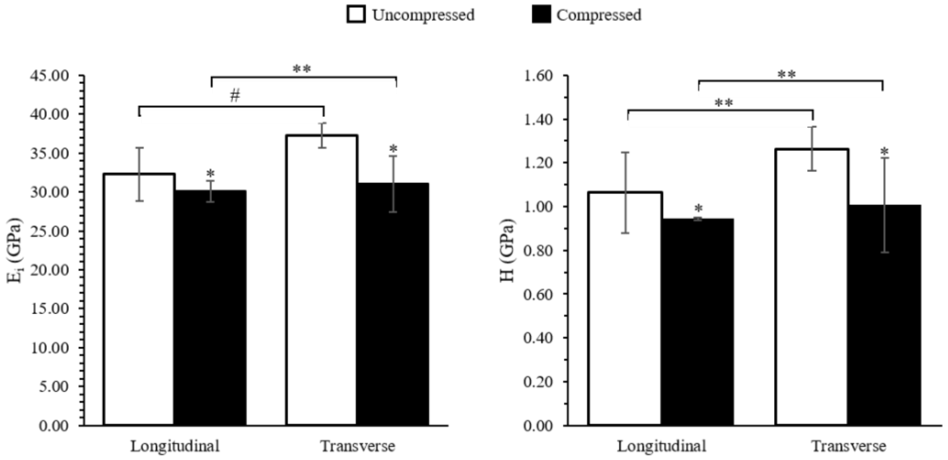

Fig.11. Indentation modulus E_i (left) and hardness H (right) before and after mechanical testing in longitudinal and transverse section. $^*p<0.001$ when comparing uncompressed to compressed values on the same section; $^{**}p<0.001$ and $^{\#}p<0.05$ when compared transversal to longitudinal values on the same mechanical condition.

4. Discussion

In this study, an innovative porous Mg-based scaffold produced by liquid-phase sintering of melt extracted Mg fibres and designed to promote bone regeneration in critical-sized defects was mechanically and morphometrically evaluated. This characterisation was conducted at different scales using *in situ* XCT mechanical testing coupled with DVC as well as electron microscopy-based methods (SEM, EBSD and EDX) and nanoindentation. The Mg scaffolds mechanical behaviour was characterized by a long strain hardening region without any apparent reduction of the stress (Fig.2). It can be assumed that beyond the deformation range tested (up to 10%), this hardening phase will be followed by a densification phase where the pores would start to collapse [68]. Jiang and He [29] compressed 45-55% porous pure Mg structures up to 60% compression with a high-speed rate of 1mm/min without any stress reduction. It therefore seemed that porous Mg scaffolds can withstand high deformation without global failure.

Trabecular bone displayed its typical mechanical behaviour, with a linear elastic region followed by an increasing plastic deformation and failure. Based on the mechanical curves (Fig.2), the elastic-plastic transition in bone occurred between 3-4% compression. This was consistent with the DVC third principal strain (ε_{p3}) maps (Fig.5Ib), where, at 3% compression, the local areas approached -9000με and thus reached tissue yielding [69,70]. Moreover, microcracks were visible on higher magnification DVC maps, at 6% compression (Fig.6IIc), when bone failed (Fig.2). Similar results in term of strain magnitude and distribution have been previously found in trabecular bone specimens extracted from vertebral body [32], condyles [30] and femoral diaphysis [34].

The apparent yield stress (2.06 ± 0.87MPa) and Young's modulus (0.068 ± 0.028GPa) of Mg, in this study, were comparable to other Mg scaffolds in literature. Hedayati et al. [26] reported yield stress and Young's modulus of 1.70MPa and 0.03GPa for 80% porous Mg-Mn alloys, whereas Toghyani et al. [71] obtained values of 7.3MPa and 0.12GPa for 60% porous pure Mg scaffolds coated with an MgF_2 layer. Zhang et al. [49] achieved an even higher yield stress and Young's modulus, 22.67MPa and 0.23GPa, for less porous (35-55%) pure Mg scaffolds. In the present study, the yield stress for Mg was three to five times lower than Tb and CCTb, respectively (6.67 ± 1.75MPa and 9.77 ± 1.04MPa), as was the Young's modulus (0.29 ± 0.08GPa and 0.41 ± 0.15GPa for Tb and CCTb, respectively) (Table 1). However, these values were still within the range of trabecular bone reported in literature; 0.01-2GPa for Young's modulus and 0.2-80MPa for yield stress [72].

The accumulated strain by Mg visualised at fibre/tissue level was of the same order of magnitude as for Tb, but whilst it was largely spread over the Mg specimens (Fig.4 and 6I), leading to the overall buckling of the structure at apparent level, a more localised distribution was observed for Tb (Fig.5I and 6II), resulting in a large local strain variation between Mg and Tb at apparent level (-13658 ± 5485με and -3005 ± 1308με at 6% for Mg and Tb, respectively) (Fig.4c and 5Ic). Additionally, the fact that Mg tended more towards the CCTb mechanical pattern, which is physiologically found in the proximity of bone defects, than Tb (Fig.2, 4 and 5II) seemed to corroborate a suitable mechanical ability for critical-sized defects. Thus, although the Mg mechanical properties (e.g. Young's modulus, yield stress) appeared to be lower than those of the bone tissues tested, its ability to deform without failing or forming microcracks at fibre/material level allowed the scaffold to accumulate higher strain. This ability to deform without fracture would be beneficial to prevent premature failure, especially during the first days of implantation, when the corrosion rate of Mg scaffolds is highest and the bone callus is forming [25], and would also lead to a more uniform strain distribution providing a better mechanical stimulus for bone regeneration [3,73,74]. Furthermore, the strain range employed to deform the Mg scaffolds exceeded, by one order of magnitude, the physiological strain of bone tissue generated in daily activities such as walking or running (500-2000με) [75], suggesting that, in theory, the scaffold could also endure any high-intensity impact.

The majority of morphometric parameters computed for Mg scaffolds fell within the range of trabecular bone [76,77] (Table 2). The two exceptions were connectivity, 38.4 ± 2.4mm^{-3} for Mg compared to a range of 1.3-4.8mm^{-3} for trabecular bone [78] and pore size, 550 ± 10µm for Mg compared to 1000µm for trabecular bone [79], as these two parameters must be kept within specific limits to bone scaffolds to allow appropriate osteoconductivity and therefore facilitate tissue regeneration [80,81]. Chang et al. [81] have shown, by *in vivo* implantation of porous hydroxyapatite blocks, that mineralized lamellar bone tissue was obtained with a pore size of 300-500µm. In fact, optimal pore size combined with a highly connected porous structure facilitates cell migration and bridging of bone fragments at the injured site [80]. Thus, the fully interconnected Mg structure and 550µm average pore size would offer the ideal 3D environment to promote critical-sized bone defect healing (Fig.3). Furthermore, a two-fold reduction in Mg pore diameter compared to trabecular bone resulted in a four-fold reduction in the load above which the fibres/trabeculae parallel to the load axis start to buckle and then fail [82]. Thus, the presence of smaller pores in the Mg structure contributed to a more efficient load transfer, preventing microcrack formation at fibre level [83]. Porosity is also strongly involved in the overall mechanical behaviour of highly connected Mg porous scaffolds. Mg structures with an overall porosity lower than 40-42% tend to be more brittle and exhibit shear behaviour with cracks along the maximum shear stress, while the porosity of the Mg scaffolds herein presented (50-60%) promotes a more ductile densification behaviour, thus tending towards optimised mechanical performances [84].

In order to further understand the Mg strain distribution, a local morphometric analysis was performed by targeting potential differences related to strain variations. Based on a direct comparison between high (exceeding the absolute strain of 40000με) and low (not exceeding the absolute strain of 10000με) strain regions, it was found that higher local porosity (fibre/trabecular spacing from 248µm to 217µm with connectivity from 38.8mm^{-3} to 45.1mm^{-3}, for high and low-strain, respectively) contributed to higher local strain (Table 3), as previously observed for trabecular bone [85], bone-biomaterial systems [86] and metallic foams [83], where microarchitecture plays a fundamental role in their load-transfer mechanism. Thus, suggesting how a local variation of the morphometric properties led to a higher local deformation (Fig.4) that in turn guided the mechanical behaviour of the structure at apparent level.

At the grain level, the EBSD results highlighted how some fibres were made of one single grain (Fig.9b) and thus, their microstructure seemed not to be subject to grain refinement due to the melt extraction process used, which allows rapid solidification and consequently a relatively homogeneous grain structure [50,51]. However, grain refinement was also observed in most fibres (Fig.8 and 9) as a consequence of the use of liquid-sintering to fuse the fibres. Furthermore, although no microcracks were observed in the XCT images after mechanical testing, some defects could be detected by electron microscopy (Fig.7e and g) prior to compression at the fibre junction, resulting from incomplete fusion between two fibres due to the accumulation of Y-Zn-rich particles and causing higher deformation areas after compression (Fig.7h). The accumulation of such Y-Zn-rich particles was also found at the grain boundary (Fig. 10b), which is typical of the liquid-sintering process and has already been observed for various Mg alloys [26,47,87]. In particular, the significant impact of sintering conditions and especially the temperature was previously studied by Zhou et al. [87], where an increase in sintering temperature affected the distribution of the β-$Mg_{17}Al_{12}$ phase particles, more abundant along the grain boundary for

AZ91 scaffolds. Thus, it could be observed how the sintering process was responsible for microdefects (i.e. grain refinement and incomplete melting at the fibre junction) by promoting the precipitation of Y-Zn-rich particles within the Mg-based scaffold (Fig. 10b). However, it has been shown that, despite the accumulation of such particles at the fibre junctions in MgY4 (W4) alloys, the fibre bonds were still strong enough to avoid dislocation [18,50,51]. This was consistent with the results of this study, as no differences were observed after compression at the grain level (Fig.8f and 9g).

Additionally, it appeared that only the fibres in the transverse section were plastically strained prior to mechanical testing during the sintering process (Fig.8 and 9). This induced a higher hardness and indentation modulus in the transverse section before compression at the nanoscale (Fig.11), reflecting how plastic deformation during the manufacturing process induced fibre anisotropy and changed their mechanical behaviour. The anisotropic ratio of 1.2 was relatively close to that of the trabecular bone (about 1.6), obtained by nanoindentation on undeformed trabeculae [42]. After mechanical testing, the indentation modulus and hardness of Mg were further reduced along the transverse section (17 and 20% of reduction, respectively), compared to the longitudinal (7 and 11% of reduction, respectively). It was therefore assumed that microdamage occurred on the crystallographic level along the directional solidification of the fibres during the melt-extraction process. In addition, the liquid-sintering process by initiating Y-Zn-rich particles precipitation and microdefects formation, also contributed to the reduction of mechanical properties locally. The indentation modulus and hardness of Mg were relatively similar to those obtained by Witte et al. [39] for Al-Zn-Mg alloys (AZ91D) with hydroxyapatite particles as reinforcements (40GPa), as well as for others Mg-based alloys [43–45], but slightly higher than trabecular bone (15 to 20GPa) [41].

The set of results presented in this study highlight the importance of a multi-scale examination of Mg-based scaffolds to better understand their mechanical behaviour after implantation and provide evidence that these scaffolds could be biomechanically suitable to act as a bone treatment for critical-sized defects. However, this study has not explored the impact of corrosion on the mechanical and morphological properties of the scaffolds. Several authors have pointed out the crucial importance of tuning the corrosion rate with the bone regeneration ability in order to ensure sufficient mechanical support of the scaffold until the bone is fully restored [6,11,24,25]. A substantial deterioration in mechanical properties (e.g. Young's modulus, yield stress) was observed when pure Mg scaffolds were immersed in simulated body fluid (SBF) *in vitro* and then mechanically compressed [88,89]. On the other hand, the use of specific chemical elements such as Y and Zn has been shown to significantly contribute to the strengthening of Mg-based scaffolds [24,25]. Li et al. [90] measured the variation in mechanical properties of Y-RE-Mg (WE43) alloys after *in vitro* corrosion in revised SBF. It was observed that the yield stress remained relatively constant up to 14 days, followed by a decrease at 28 days (from 23MPa to 15MPa) while Young's modulus increased during the first days of immersion, then decreased after 7 days to a value similar to that measured before immersion. The change in mechanical properties was mainly attributed to an increase in the amount of corrosion products and structural changes in some severely degraded struts. These results suggest that the Mg-based scaffolds herein studied should maintain their mechanical integrity after corrosion during the first days post-operatively, given that Y and Zn are part of their alloying composition. Subsequently, the bone tissue, guided by the Mg scaffold, will regenerate *in vivo* [18–22,54] providing a mechanically compliant bone-biomaterial system to counterbalance the decline in mechanical properties of Mg-alloy due to corrosion and to sustain the load up to the full bone restoration.

Another major challenge concerning Mg-based implants relates to the *in vivo* release of hydrogen gas due to excessive corrosion rates [11]. In a similar scaffold design made of uncoated MgY4 alloy, Bobe et al. [18] observed the presence of gas cavities in proximity of the scaffolds 6 weeks post-implantation in a rabbit femoral condyle model, corresponding to a higher corrosion rate (0.6mm/year). However, after 12 weeks, the corrosion rate decreased to 0.08mm/year resulted in the absence of gas cavities; thus, suggesting control of hydrogen formation. Moreover, surface treatments and coating of the scaffolds are known to reduce the corrosion rates and thus, the evolution of hydrogen gas without impairing the mechanical properties [91]. Therefore, further investigation should be conducted accordingly to evaluate the mechanical and morphological changes in such Mg-based scaffolds following controlled *in vitro* as well as *in vivo* corrosion to fully characterize their suitability for the treatment of critical-sized bone defects.

5. Conclusions

This study aimed to fully characterise the morphological and mechanical properties of open-porous Mg-based (WZM211) scaffolds produced by sintering in order to evaluate their biomechanical suitability as bone substitutes in critical-sized defects. Various techniques, including *in situ* mechanical testing coupled with XCT imaging and digital volume correlation (DVC), electron-based microscopy and nanoindentation were successfully applied, allowing a multi-scale evaluation of these scaffolds. The results showed that at apparent level, the Mg scaffold exhibited slightly lower mechanical properties than trabecular bone but was highly ductile and able to accumulate a considerable amount of strain without global failure, while trabecular bone developed microcracks for similar strain levels. This behaviour could be explained by its highly connected porous network, which contributed to a more efficient load transfer at Mg fibre level. Ultimately, the investigated Mg porous scaffolds represent a valid bone replacement, capable of sustaining mechanical loads *in situ* during the first post-operative phase.

Acknowledgements

The authors gratefully acknowledge Dr Jurgita Zekonyte for her assistance during the nanoindentation testing and Dr James Darling for his valuable advice on the EBSD data analysis. We further acknowledge the Zeiss Global Centre (University of Portsmouth) for providing XCT image acquisition facilities and DVC software. This study was part of a PhD programme co-funded by Biotrics bioimplants GmBH (Berlin, Germany), the German Federal Ministry of Education and Research (BMBF, grant number 13GW0176A) and the University of Portsmouth (Portsmouth, United Kingdom).

References

[1] A. Oryan, S. Monazzah, A. Bigham-Sadegh, Bone injury and fracture healing biology, Biomed. Environ. Sci. 28 (2015) 57–71. https://doi.org/10.3967/bes2015.006.

[2] W. Wang, K.W.K. Yeung, Bone grafts and biomaterials substitutes for bone defect repair: A review, Bioact. Mater. 2 (2017) 224–247. https://doi.org/10.1016/j.bioactmat.2017.05.007.

[3] M. Koolen, S.A. Yavari, K. Lietaert, R. Wauthle, A.A. Zadpoor, H. Weinans, Bone regeneration in critical-sized bone defects treated with additively manufactured porous metallic biomaterials: The effects of inelastic mechanical properties, Materials (Basel). 13 (2020). https://doi.org/10.3390/MA13081992.

[4] Y. Guo, K. Xie, W. Jiang, L. Wang, G. Li, S. Zhao, W. Wu, Y. Hao, In Vitro and in Vivo Study of 3D-Printed Porous Tantalum Scaffolds for Repairing Bone Defects, ACS Biomater. Sci. Eng. 5 (2019) 1123–1133. https://doi.org/10.1021/acsbiomaterials.8b01094.

[5] H.S. Sohn, J.K. Oh, Review of bone graft and bone substitutes with an emphasis on fracture surgeries, Biomater. Res. 23 (2019) 4–10. https://doi.org/10.1186/s40824-019-0157-y.

[6] D. Zhao, F. Witte, F. Lu, J. Wang, J. Li, L. Qin, Current status on clinical applications of magnesium-based orthopaedic implants : A review from clinical translational perspective, Biomaterials. 112 (2017) 287–302. https://doi.org/10.1016/j.biomaterials.2016.10.017.

[7] W.R. Walsh, R.A. Oliver, C. Christou, V. Lovric, E.R. Walsh, G.R. Prado, T. Haider, Critical size bone defect healing using collagen-calcium phosphate bone graft materials, PLoS One. 12 (2017) 1–21. https://doi.org/10.1371/journal.pone.0168883.

[8] F. Baino, S. Hamzehlou, S. Kargozar, Bioactive glasses: Where are we and where are we going?, J. Funct. Biomater. 9 (2018). https://doi.org/10.3390/jfb9010025.

[9] G. Tozzi, A. De Mori, A. Oliveira, M. Roldo, Composite hydrogels for bone regeneration, Materials (Basel). 9 (2016) 1–24. https://doi.org/10.3390/ma9040267.

[10] R.Y. Basha, S.T.S. Kumar, M. Doble, Design of biocomposite materials for bone tissue

regeneration, Mater. Sci. Eng. C. 57 (2015) 452–463. https://doi.org/10.1016/j.msec.2015.07.016.

[11] F. Witte, Reprint of: The history of biodegradable magnesium implants: A review, Acta Biomater. 23 (2015) S28–S40. https://doi.org/10.1016/j.actbio.2015.07.017.

[12] B. Jahani, K. Meesterb, X. Wanga, A. Brooks, Biodegradable Magnesium-Based Alloys for Bone Repair Applications : Prospects and, Biomed Sci Instrum. 56 (2020) 292–304.

[13] W. Jahnen-Dechent, M. Ketteler, Magnesium basics, Clin. Kidney J. 5 (2012) 3–14. https://doi.org/10.1093/ndtplus/sfr163.

[14] F.I. Wolf, A. Cittadini, Chemistry and biochemistry of magnesium, Mol. Aspects Med. 24 (2003) 3–9. https://doi.org/10.1016/S0098-2997(02)00087-0.

[15] M. Haseeb, M.F. Butt, T. Altaf, K. Muzaffar, A. Gupta, A. Jallu, Indications of implant removal: A study of 83 cases., Int. J. Health Sci. (Qassim). 11 (2017) 1–7.

[16] H. May, Y. Alper Kati, G. Gumussuyu, T. Yunus Emre, M. Unal, O. Kose, Bioabsorbable magnesium screw versus conventional titanium screw fixation for medial malleolar fractures, J. Orthop. Traumatol. 21 (2020) 4–11. https://doi.org/10.1186/s10195-020-00547-7.

[17] F. Schwarz, M. Langer, T. Hagena, B. Hartig, R. Sader, J. Becker, Cytotoxicity and proinflammatory effects of titanium and zirconia particles, Int. J. Implant Dent. 5 (2019) 4–9. https://doi.org/10.1186/s40729-019-0178-2.

[18] K. Bobe, E. Willbold, I. Morgenthal, O. Andersen, T. Studnitzky, J. Nellesen, W. Tillmann, C. Vogt, K. Vano, F. Witte, In vitro and in vivo evaluation of biodegradable, open-porous scaffolds made of sintered magnesium W4 short fibres, Acta Biomater. 9 (2013) 8611–8623. https://doi.org/10.1016/j.actbio.2013.03.035.

[19] F. Witte, V. Kaese, H. Haferkamp, E. Switzer, A. Meyer-Lindenberg, C.J. Wirth, H. Windhagen, In vivo corrosion of four magnesium alloys and the associated bone response, Biomaterials. 26 (2005) 3557–3563. https://doi.org/10.1016/j.biomaterials.2004.09.049.

[20] F. Witte, H. Ulrich, M. Rudert, E. Willbold, Biodegradable magnesium scaffolds: Part I: Appropriate inflammatory response, J. Biomed. Mater. Res. Part A. 81 (2007) 748–756. https://doi.org/10.1002/jbm.a.31170.

[21] F. Witte, H. Ulrich, C. Palm, E. Willbold, Biodegradable magnesium scaffolds: Part II: Peri-implant bone remodeling, J. Biomed. Mater. Res. Part A. 81 (2007) 757–765. https://doi.org/10.1002/jbm.a.31293.

[22] H. Han, I. Jun, H. Seok, K. Lee, K. Lee, F. Witte, D. Mantovani, Y. Kim, S. Glyn-Jones, J.R. Edwards, Biodegradable Magnesium Alloys Promote Angio-Osteogenesis to Enhance Bone Repair, Adv. Sci. 7 (2020) 1–12. https://doi.org/10.1002/advs.202000800.

[23] F. Schmidutz, Y. Agarwal, P.E. Müller, B. Gueorguiev, R.G. Richards, C.M. Sprecher, Stress-shielding induced bone remodeling in cementless shoulder resurfacing arthroplasty: A finite element analysis and in vivo results, J. Biomech. 47 (2014) 3509–3516. https://doi.org/10.1016/j.jbiomech.2014.08.029.

[24] Q. Chen, G.A. Thouas, Metallic implant biomaterials, Mater. Sci. Eng. R. 87 (2015) 1–57. https://doi.org/10.1016/j.mser.2014.10.001.

[25] Y.F.F. Zheng, X.N.N. Gu, F. Witte, Biodegradable metals, Mater. Sci. Eng. R Reports. 77 (2014) 1–34. https://doi.org/10.1016/j.mser.2014.01.001.

[26] R. Hedayati, S.M. Ahmadi, K. Lietaert, N. Tümer, Y. Li, S. Amin Yavari, A.A. Zadpoor, Fatigue and quasi-static mechanical behavior of bio-degradable porous biomaterials based on magnesium alloys, J. Biomed. Mater. Res. Part A. 106 (2018) 1798–1811. https://doi.org/10.1002/jbm.a.36380.

[27] S.H. Byun, H.K. Lim, K.H. Cheon, S.M. Lee, H.E. Kim, J.H. Lee, Biodegradable magnesium

alloy (WE43) in bone-fixation plate and screw, J. Biomed. Mater. Res. - Part B Appl. Biomater. 108 (2020) 2505–2512. https://doi.org/10.1002/jbm.b.34582.

[28] T. Guillén, Q. Zhang, G. Tozzi, A. Ohrndorf, H. Christ, J. Tong, Compressive behaviour of bovine cancellous bone and bone analogous materials , microCT characterisation and FE analysis, J. Mech. Behav. Biomed. Mater. 4 (2011) 1452–1461. https://doi.org/10.1016/j.jmbbm.2011.05.015.

[29] G. Jiang, G. He, A new approach to the fabrication of porous magnesium with well-controlled 3D pore structure for orthopedic applications, Mater. Sci. Eng. C. 43 (2014) 317–320. https://doi.org/10.1016/j.msec.2014.07.033.

[30] M. Peña Fernández, E. Dall'Ara, A.J. Bodey, R. Parwani, A.H. Barber, G.W. Blunn, G. Tozzi, Full-Field Strain Analysis of Bone-Biomaterial Systems Produced by the Implantation of Osteoregenerative Biomaterials in an Ovine Model, ACS Biomater. Sci. Eng. 5 (2019) 2543–2554. https://doi.org/10.1021/acsbiomaterials.8b01044.

[31] F. Gillard, R. Boardman, M. Mavrogordato, D. Hollis, I. Sinclair, F. Pierron, M. Browne, The application of digital volume correlation (DVC) to study the microstructural behaviour of trabecular bone during compression, J. Mech. Behav. Biomed. Mater. 29 (2014) 480–499. https://doi.org/10.1016/j.jmbbm.2013.09.014.

[32] G. Tozzi, V. Danesi, M. Palanca, L. Cristofolini, Elastic Full-Field Strain Analysis and Microdamage Progression in the Vertebral Body from Digital Volume Correlation, Strain. 52 (2016) 446–455. https://doi.org/10.1111/str.12202.

[33] B.C. Roberts, E. Perilli, K.J. Reynolds, Application of the digital volume correlation technique for the measurement of displacement and strain fields in bone: A literature review, J. Biomech. 47 (2014) 923–934. https://doi.org/10.1016/j.jbiomech.2014.01.001.

[34] A. Karali, A.P. Kao, R. Meeson, M. Roldo, G.W. Blunn, G. Tozzi, Full-field strain of regenerated bone tissue in a femoral fracture model, J. Microsc. 00 (2020) 1–11. https://doi.org/10.1111/jmi.12937.

[35] G. Tozzi, M. Peña Fernández, S. Davis, A. Karali, A.P. Kao, G. Blunn, Full-Field Strain Uncertainties and Residuals at the Cartilage-Bone Interface in Unstained Tissues Using Propagation-Based Phase-Contrast XCT and Digital Volume Correlation, Materials (Basel). 13 (2020) 2579. https://doi.org/10.3390/ma13112579.

[36] K. Madi, G. Tozzi, Q.H. Zhang, J. Tong, A. Cossey, A. Au, D. Hollis, F. Hild, Computation of full-field displacements in a scaffold implant using digital volume correlation and finite element analysis, Med. Eng. Phys. 35 (2013) 1298–1312. https://doi.org/10.1016/j.medengphy.2013.02.001.

[37] G. Tozzi, Q.H. Zhang, J. Tong, Microdamage assessment of bone-cement interfaces under monotonic and cyclic compression, J. Biomech. 47 (2014) 3466–3474. https://doi.org/10.1016/j.jbiomech.2014.09.012.

[38] M. Peña Fernández, F. Witte, G. Tozzi, Applications of X-ray computed tomography for the evaluation of biomaterial-mediated bone regeneration in critical-sized defects, J. Microsc. 277 (2019) 179–196. https://doi.org/10.1111/jmi.12844.

[39] F. Witte, F. Feyerabend, P. Maier, J. Fischer, M. Störmer, C. Blawert, W. Dietzel, N. Hort, Biodegradable magnesium-hydroxyapatite metal matrix composites, Biomaterials. 28 (2007) 2163–2174. https://doi.org/10.1016/j.biomaterials.2006.12.027.

[40] R. Zhang, H. Gong, D. Zhu, J. Gao, J. Fang, Y. Fan, Seven day insertion rest in whole body vibration improves multi-level bone quality in tail suspension rats, PLoS One. 9 (2014). https://doi.org/10.1371/journal.pone.0092312.

[41] J.Y. Rho, M.E. Roy, T.Y. Tsui, G.M. Pharr, Elastic properties of microstructural components of human bone tissue as measured by nanoindentation, J. Biomed. Mater. Res. 45 (1999) 48–

54. https://doi.org/10.1002/(SICI)1097-4636(199904)45:1<48::AID-JBM7>3.0.CO;2-5.

[42] M. Casanova, A. Balmelli, D. Carnelli, D. Courty, P. Schneider, R. Müller, Nanoindentation analysis of the micromechanical anisotropy in mouse cortical bone, R. Soc. Open Sci. 4 (2017). https://doi.org/10.1098/rsos.160971.

[43] A.K. Gartzke, S. Julmi, C. Klose, S. Besdo, A.C. Waselau, A. Meyer-Lindenberg, H.J. Maier, P. Wriggers, Investigation of degraded bone substitutes made of magnesium alloy using scanning electron microscope and nanoindentation, J. Mech. Behav. Biomed. Mater. 109 (2020) 103825. https://doi.org/10.1016/j.jmbbm.2020.103825.

[44] L. Wolters, S. Besdo, N. Angrisani, P. Wriggers, B. Hering, J.M. Seitz, J. Reifenrath, Degradation behaviour of LAE442-based plate-screw-systems in an in vitro bone model, Mater. Sci. Eng. C. 49 (2015) 305–315. https://doi.org/10.1016/j.msec.2015.01.019.

[45] B. Ratna Sunil, C. Ganapathy, T.S. Sampath Kumar, U. Chakkingal, Processing and mechanical behavior of lamellar structured degradable magnesium-hydroxyapatite implants, J. Mech. Behav. Biomed. Mater. 40 (2014) 178–189. https://doi.org/10.1016/j.jmbbm.2014.08.016.

[46] S. Sanyal, S. Kanodia, R. Saha, T.K. Bandyopadhyay, S. Mandal, Influence of hard plate hot forging temperature on the microstructure, texture and mechanical properties in a lean Mg–Zn–Al alloy, J. Alloys Compd. 800 (2019) 343–354. https://doi.org/10.1016/j.jallcom.2019.06.026.

[47] Y. Li, H. Jahr, X.Y. Zhang, M.A. Leeflang, W. Li, B. Pouran, F.D. Tichelaar, H. Weinans, J. Zhou, A.A. Zadpoor, Biodegradation-affected fatigue behavior of additively manufactured porous magnesium, Addit. Manuf. 28 (2019) 299–311. https://doi.org/10.1016/j.addma.2019.05.013.

[48] N. Zou, Q. Li, Mechanical Properties of Lightweight Porous Magnesium Processed Through Powder Metallurgy, J. Miner. Met. Mater. Soc. 70 (2018) 650–655. https://doi.org/10.1007/s11837-018-2772-9.

[49] X. Zhang, X. Li, J. Li, X. Sun, Preparation and mechanical property of a novel 3D porous magnesium scaffold for bone tissue engineering, Mater. Sci. Eng. C. 42 (2014) 362–367. https://doi.org/10.1016/j.msec.2014.05.044.

[50] T. Studnitzky, O. Andersen, I. Morgenthal, G. Stephani, B. Kieback, Sintering of aluminium and magnesium alloy fiber structures, Euro Int. Powder Metall. Congr. Exhib. (2011) 345–350.

[51] I. Morgenthal, O. Andersen, C. Kostmann, G. Stephani, T. Studnitzky, F. Witte, B. Kieback, Highly porous magnesium alloy structures and their properties regarding degradable implant application, Adv. Eng. Mater. 16 (2014) 309–318. https://doi.org/10.1002/adem.201300130.

[52] J.D. Currey, The many adaptations of bone, J. Biomech. 36 (2003) 1487–1495. https://doi.org/10.1016/S0021-9290(03)00124-6.

[53] T.M. Keaveny, T.P. Pinilla, R.P. Crawford, D.L. Kopperdahl, A. Lou, Systematic and random errors in compression testing of trabecular bone, J. Orthop. Res. 15 (1997) 101–110. https://doi.org/10.1002/jor.1100150115.

[54] M. Peña Fernández, C. Black, J. Dawson, D. Gibbs, J. Kanczler, R.O.C. Oreffo, G. Tozzi, Exploratory full-field strain analysis of regenerated bone tissue from osteoinductive biomaterials, Materials (Basel). 13 (2020) 168. https://doi.org/10.3390/ma13010168.

[55] E. Dall'Ara, M. Peña-Fernández, M. Palanca, M. Giorgi, L. Cristofolini, G. Tozzi, Precision of Digital Volume Correlation Approaches for Strain Analysis in Bone Imaged with Micro-Computed Tomography at Different Dimensional Levels, Front. Mater. 4 (2017) 1–13. https://doi.org/10.3389/fmats.2017.00031.

[56] T.M. Keaveny, X.E. Guo, E.F. Wachtel, W.C.M. Thomas A.Hayes, Trabecular bone exhibits fully linear elastic behavior and yields at low strains, J. Biomech. 27 (1994) 1127–1136.

https://doi.org/10.1016/0021-9290(94)90053-1.

[57] A. Buades, B. Coll, J.-M. Morel, A non-local algorithm for image denoising, IEEE Comput. Soc. Conf. Comput. Vis. Pattern Recognit. 2 (2005) 60–65. https://doi.org/10.1109/ICIP.2006.312698.

[58] N. Otsu, A Threshold Selection Method from Gray-Level Histograms, IEEE Trans. Syst. Man Cybern. 9 (1979) 62–66. https://doi.org/10.1109/TSMC.1979.4310076.

[59] M. Peña Fernández, A.H. Barber, G.W. Blunn, G. Tozzi, Optimization of digital volume correlation computation in SR-microCT images of trabecular bone and bone-biomaterial systems, J. Microsc. 272 (2018) 213–228. https://doi.org/10.1111/jmi.12745.

[60] W.B. Lievers, A.C. Petryshyn, A.S. Poljsak, S.D. Waldman, A.K. Pilkey, Specimen diameter and “side artifacts” in cancellous bone evaluated using end-constrained elastic tension, Bone. 47 (2010) 371–377. https://doi.org/10.1016/j.bone.2010.03.024.

[61] M.L. Bouxsein, S.K. Boyd, B.A. Christiansen, R.E. Guldberg, K.J. Jepsen, R. Müller, Guidelines for assessment of bone microstructure in rodents using micro-computed tomography, J. Bone Miner. Res. 25 (2010) 1468–1486. https://doi.org/10.1002/jbmr.141.

[62] J. Schindelin, I. Arganda-Carreras, E. Frise, V. Kaynig, M. Longair, T. Pietzsch, S. Preibisch, C. Rueden, S. Saalfeld, B. Schmid, J.Y. Tinevez, D.J. White, V. Hartenstein, K. Eliceiri, P. Tomancak, A. Cardona, Fiji: An open-source platform for biological-image analysis, Nat. Methods. 9 (2012) 676–682. https://doi.org/10.1038/nmeth.2019.

[63] M. Doube, M.M. Klosowski, I. Arganda-Carreras, F.P. Cordelières, R.P. Dougherty, J.S. Jackson, B. Schmid, J.R. Hutchinson, S.J. Shefelbine, BoneJ: Free and extensible bone image analysis in ImageJ, Bone. 47 (2010) 1076–1079. https://doi.org/10.1016/j.bone.2010.08.023.

[64] M. Palanca, A.J. Bodey, M. Giorgi, M. Viceconti, D. Lacroix, L. Cristofolini, E. Dall’Ara, Local displacement and strain uncertainties in different bone types by digital volume correlation of synchrotron microtomograms, J. Biomech. 58 (2017) 27–36. https://doi.org/10.1016/j.jbiomech.2017.04.007.

[65] G. Tozzi, E. Dall’Ara, M. Palanca, M. Curto, F. Innocente, L. Cristofolini, Strain uncertainties from two digital volume correlation approaches in prophylactically augmented vertebrae: Local analysis on bone and cement-bone microstructures, J. Mech. Behav. Biomed. Mater. 67 (2017) 117–126. https://doi.org/10.1016/j.jmbbm.2016.12.006.

[66] W.C. Oliver, G.M. Pharr, An improved technique for determining hardness and elastic modulus using load and displacement sensing indentation experiments experiments, J. Mater. Res. 7 (1992) 1564–1583. https://doi.org/10.1557/JMR.1992.1564.

[67] H. Gercek, Poisson’s ratio values for rocks, Int. J. Rock Mech. Min. Sci. 44 (2007) 1–13. https://doi.org/10.1016/j.ijrmms.2006.04.011.

[68] L.J. Gibson, Biomechanics of cellular solids, J. Biomech. 38 (2005) 377–399. https://doi.org/10.1016/j.jbiomech.2004.09.027.

[69] D.L. Kopperdahl, T.M. Keaveny, Yield strain behavior of trabecular bone, J. Biomech. 31 (1998) 601–608. https://doi.org/10.1016/S0021-9290(98)00057-8.

[70] H.H. Bayraktar, E.F. Morgan, G.L. Niebur, G.E. Morris, E.K. Wong, T.M. Keaveny, Comparison of the elastic and yield properties of human femoral trabecular and cortical bone tissue, J. Biomech. 37 (2004) 27–35. https://doi.org/10.1016/S0021-9290(03)00257-4.

[71] S. Toghyani, M. Khodaei, M. Razavi, Magnesium scaffolds with two novel biomimetic designs and MgF2 coating for bone tissue engineering, Surf. Coatings Technol. 395 (2020) 125929. https://doi.org/10.1016/j.surfcoat.2020.125929.

[72] L.J. Gibson, The mechanical behaviour of cancellous bone, J. Biomech. 18 (1985) 317–328. https://doi.org/10.1016/0021-9290(85)90287-8.

[73] R. Weinkamer, C. Eberl, P. Fratzl, Mechanoregulation of bone remodeling and healing as inspiration for self-repair in materials, Biomimetics. 4 (2019) 1–16. https://doi.org/10.3390/biomimetics4030046.

[74] J.D. Boerckel, Y.M. Kolambkar, H.Y. Stevens, A.S.P. Lin, K.M. Dupont, R.E. Guldberg, Effects of in vivo mechanical loading on large bone defect regeneration, J. Orthop. Res. 30 (2012) 1067–1075. https://doi.org/10.1002/jor.22042.Effects.

[75] P.F. Yang, G.-P. Brüggemann, J. Rittweger, What do we currently know from in vivo bone strain measurements in humans?, J. Musculoskelet. Neuronal Interact. 11 (2011) 8–20.

[76] M. Ding, C.C. Danielsen, I. Hvid, S. Overgaard, Three-dimensional microarchitecture of adolescent cancellous bone, Bone. 51 (2012) 953–960. https://doi.org/10.1016/j.bone.2012.07.018.

[77] Y.N. Yeni, B. Wu, L. Huang, D. Oravec, Mechanical loading causes detectable changes in morphometric measures of trabecular structure in human cancellous bone, J. Biomech. Eng. 135 (2013) 1–5. https://doi.org/10.1115/1.4024136.

[78] L. Mulder, B. Van Rietbergen, N.J. Noordhoek, K. Ito, Determination of vertebral and femoral trabecular morphology and stiffness using a flat-panel C-arm-based CT approach, Bone. 50 (2012) 200–208. https://doi.org/10.1016/j.bone.2011.10.020.

[79] T.M. Keaveny, E.F. Morgan, G.L. Niebur, O.C. Yeh, Biomechanics of Trabecular Bone, Annu. Rev. Biomed. Eng. 3 (2001) 307–333. https://doi.org/10.1146/annurev.bioeng.3.1.307.

[80] V. Karageorgiou, D. Kaplan, Porosity of 3D biomaterial scaffolds and osteogenesis, Biomaterials. 26 (2005) 5474–5491. https://doi.org/10.1016/j.biomaterials.2005.02.002.

[81] B.S. Chang, C.K. Lee, K.S. Hong, H.J. Youn, H.S. Ryu, S.S. Chung, K.W. Park, Osteoconduction at porous hydroxyapatite with various pore configurations, Biomaterials. 21 (2000) 1291–1298. https://doi.org/10.1016/S0142-9612(00)00030-2.

[82] H.B. Ly, C. Desceliers, L.M. Le, T.T. Le, B.T. Pham, L. Nguyen-Ngoc, V.T. Doan, M. Le, Quantification of uncertainties on the critical buckling load of columns under axial compression with uncertain random materials, Materials (Basel). 12 (2019) 1–19. https://doi.org/10.3390/ma12111828.

[83] O. Andersen, M. Vesenjak, T. Fiedler, U. Jehring, L. Krstulović-Opara, Experimental and numerical evaluation of the mechanical behavior of strongly anisotropic light-weight metallic fiber structures under static and dynamic compressive loading, Materials (Basel). 9 (2016) 1–20. https://doi.org/10.3390/ma9050398.

[84] G. Jiang, Q. Li, C. Wang, J. Dong, G. He, Characterization and investigation of the deformation behavior of porous magnesium scaffolds with entangled architectured pore channels, J. Mech. Behav. Biomed. Mater. 64 (2016) 139–150. https://doi.org/10.1016/j.jmbbm.2016.07.008.

[85] E. Perilli, M. Baleani, C. Öhman, R. Fognani, F. Baruffaldi, M. Viceconti, Dependence of mechanical compressive strength on local variations in microarchitecture in cancellous bone of proximal human femur, J. Biomech. 41 (2008) 438–446. https://doi.org/10.1016/j.jbiomech.2007.08.003.

[86] G. Tozzi, Q.H. Zhang, J. Tong, 3D real-time micromechanical compressive behaviour of bone-cement interface: Experimental and finite element studies, J. Biomech. 45 (2012) 356–363. https://doi.org/10.1016/j.jbiomech.2011.10.011.

[87] Y.J. Zhou, A.Y. Jiang, J.X. Liu, The effect of sintering temperature to the microstructure and properties of AZ91 magnesium alloy by powder metallurgy, Appl. Mech. Mater. 377 (2013) 250–254. https://doi.org/10.4028/www.scientific.net/AMM.377.250.

[88] A. Putra Md Saad, N. Jasmawati, M.N. Harun, M.R.A. Kadir, H. Nur, H. Hermawan, A. Syahrom, Dynamic degradation of porous magnesium under a simulated environment of

human cancellous bone, Corros. Sci. 112 (2016) 495–506. https://doi.org/10.1016/j.corsci.2016.08.017.

[89] H. Basri, A.T. Prakoso, M.A. Sulong, A.P. Md Saad, M.H. Ramlee, D. Agustin Wahjuningrum, S. Sipaun, A. Öchsner, A. Syahrom, Mechanical degradation model of porous magnesium scaffolds under dynamic immersion, Proc. Inst. Mech. Eng. Part L J. Mater. Des. Appl. 234 (2020) 175–185. https://doi.org/10.1177/1464420719881736.

[90] Y. Li, J. Zhou, P. Pavanram, M.A. Leeflang, L.I. Fockaert, B. Pouran, N. Tümer, K.U. Schröder, J.M.C. Mol, H. Weinans, H. Jahr, A.A. Zadpoor, Additively manufactured biodegradable porous magnesium, Acta Biomater. 67 (2018) 378–392. https://doi.org/10.1016/j.actbio.2017.12.008.

[91] H. Hornberger, S. Virtanen, A.R. Boccaccini, Biomedical coatings on magnesium alloys - A review, Acta Biomater. 8 (2012) 2442–2455. https://doi.org/10.1016/j.actbio.2012.04.012.